Research Article Vol. 10, No. 3 / March 2023 / Optica 407

Full-field quantitative X-ray phase nanotomography via space-domain Kramers–Kronig relations

KyeoReh Lee,[1,2,*] Jun Lim,[3,5] and YongKeun Park[1,2,4,6]

[1]Department of Physics, Korea Advanced Institute of Science and Technology, Daejeon 34141, Republic of Korea
[2]KAIST Institute for Health Science and Technology, Korea Advanced Institute of Science and Technology, Daejeon, 34141, Republic of Korea
[3]Pohang Accelerator Laboratory, Pohang University of Science and Technology, Pohang, Kyungbuk 37637, Republic of Korea
[4]Tomocube Inc., Daejeon 34051, Republic of Korea
[5]limjun@postech.ac.kr
[6]yk.park@kaist.ac.kr
*kyeo@kaist.ac.kr

Received 21 November 2022; revised 2 February 2023; accepted 17 February 2023; published 9 March 2023

Given the low absorption contrast of X-rays, phase shift has been playing an important role as an alternative source of contrast in X-ray nanoimaging. Numerous phase-measuring techniques have been proposed, most of which, however, are based on significant assumptions or sample translations. In this study, we propose the application of Kramers–Kronig (KK) relations in the spatial domain as a solution to allow the X-ray quantitative phase image to be directly calculated from the measured intensity image without any additional requirements. Based on this straightforward principle, we have presented KK nanotomography by introducing a spatial-frequency cutoff filter into a conventional tomographic setup. The robustness and versatility of the proposed method were experimentally verified based on various sample tomograms. We expect KK nanotomography to be widely adopted as a powerful and easy-to-adapt phase quantification solution for X-ray microscopes. © 2023 Optica Publishing Group under the terms of the Optica Open Access Publishing Agreement

https://doi.org/10.1364/OPTICA.481451

1. INTRODUCTION

X-ray nanotomography is a unique imaging tool that explores the three-dimensional (3-D) structure of submillimeter-sized samples at nanometer resolutions [1]. The internal nanostructures of samples can be visualized non-destructively, which is a characteristic advantage of nanotomography over electron microscopy [2,3]. The high penetrability of X-rays, however, also corresponds to the weak absorption of X-rays in matter [4]. Various materials present similar attenuation coefficients (μ) and are often indistinguishable via simple transmittance ($e^{-\mu d}$) measurements, especially when the feature size (d) is on the nanometer scale. This challenge becomes more severe for higher photon energies that exceed the absorption bands of materials [5].

To further enhance contrast of X-ray imaging, X-ray phase shift has emerged as an alternative source of contrast [6,7]. The phase shift typically provides several more orders of contrast than absorption, unless the photon energy is near the absorption edges [8,9]. Various X-ray phase tomography techniques have been proposed including interferometer-based [10], grating-based [11], propagation-based [12–15], speckle-based [16,17], and Zernike phase contrast (ZPC) [18]. Unfortunately, a few phase tomography techniques have currently been implemented for nanotomography mainly limited by the micrometer-sized detector pixels.

One popular nanotomography setup is the introduction of ZPC idea into transmission X-ray microscopy (TXM) [19–23]. The phase shift can be visualized by introducing a phase plate (or ring) near the focal plane of the lens. However, despite vivid contrast enhancement, the ZPC scheme cannot usually provide a sample phase shift in radians without employing a single-material approximation [24] or through multiple phase-shifting measurements [25,26]. Instead, it provides a mixed response of absorption and phase shift, which cannot be decoupled unless both effects are sufficiently weak [27]. Thus, unlike conventional absorption-contrast nanotomography, the sample tomogram cannot be interpreted as the physical quantity of a sample. Such an ambiguous representation is a significant drawback of ZPC nanotomography, which impedes the quantitative analysis of samples.

Another popular approach is holotomography [12]. In nanoholotomography setups, sample magnification is achieved by introducing a divergent illumination beam and sufficient propagation after the sample [12,15,28,29]. The phase values are calculated from to three to four defocused images at different distances through coherent transfer function (CTF) analysis [12,30]. However, the retrieved phase is often far from the physical phase shifts because the CTF-based phase retrieval is also based on the weak absorption and slowly varying phase approximation [30,31].

Corrected 05 April 2023

Quantitative X-ray phase nanotomography has recently been realized using ptychography [9,32–34]. The quantitative real-part refractive index of samples was visualized in 3-D and interpreted as electron densities [32,33]. The ptychographic tomography clearly demonstrates the potential advantages of quantitative X-ray phase nanotomography in various applications. However, the scanning measurements of far-field diffraction patterns for each rotation angle usually require a considerable acquisition time to generate a single tomogram. For instance, [33] utilized 245 scanning points for each projection out of 1200 angles requiring 20 h of measurement, excluding the phase retrieval and tomogram reconstruction times. This not only results in low throughput; maintaining nanometer-order stability throughout the day remains difficult even for modern synchrotron facilities [35].

To alleviate the various difficulties currently associated with quantitative X-ray phase tomography, we introduce Kramers–Kronig (KK) nanotomography in this study. We retrieved a quantitative phase directly from a measured intensity image without sample approximations or sample scanning. We exploited the space-domain KK relations instead, which is enabled by introducing a cutoff filter to the conventional TXM. Based on the theory, quantitative real-part refractive index tomograms of various samples were successfully acquired by rotating samples without any additional mechanically moving parts.

2. PRINCIPLE

A. Space-Domain KK Relation

Let $\psi(x)$ be a complex function of position x and the space-domain KK relation be

$$\psi_{\mathrm{I}}(x) = \mathrm{H}(\psi_{\mathrm{R}})(x), \tag{1}$$

where ψ_{R} and ψ_{I} are the real and imaginary parts of $\psi(x)$, respectively, and $\mathrm{H}(f)(x)$ is the Hilbert transform of $f(x)$. This is the space-domain KK relation connecting the real (ψ_{R}) and imaginary (ψ_{I}) parts of a spatial function, $\psi(x)$. It should not be confused with the conventional (frequency-domain) KK relation that links the real and imaginary susceptibility (or refractive index) of a material [36,37].

The real-imaginary relation can be switched to amplitude-phase mode by introducing a logarithm. Substituting $\psi = \log U$ into Eq. (1), we obtain $\psi_{\mathrm{R}} = \frac{1}{2}\log I$ and $\psi_{\mathrm{I}} = \varphi$ for $U(x) = \sqrt{I}e^{i\varphi}$. Thus, if we consider $U(x)$ to be a sample field, Eq. (1) directly enables the unique determination of phase $\varphi(x)$ from the measured intensity $I(x)$, which is the common objective of various phase retrieval methodologies [38–41].

B. Role of a Cutoff Filter

It should be noted that the KK relations are not universal formulas. The relations are only valid for an *analytic* signal that, by definition, does not possess negative frequency components [42]. Thus, Eq. (1) holds if and only if its Fourier transform $\tilde{\psi}(u)$ is zero for $u < 0$, where u denotes the corresponding spatial frequency. This is analogous to frequency-domain KK relations based on the causality of physical response functions, which cannot have negative time components [43].

In this study, we achieved space-domain analyticity through the introduction of a cutoff filter [Fig. 1(a)]. The filter was placed near the back-focal plane of a zone plate, where the Fourier transform

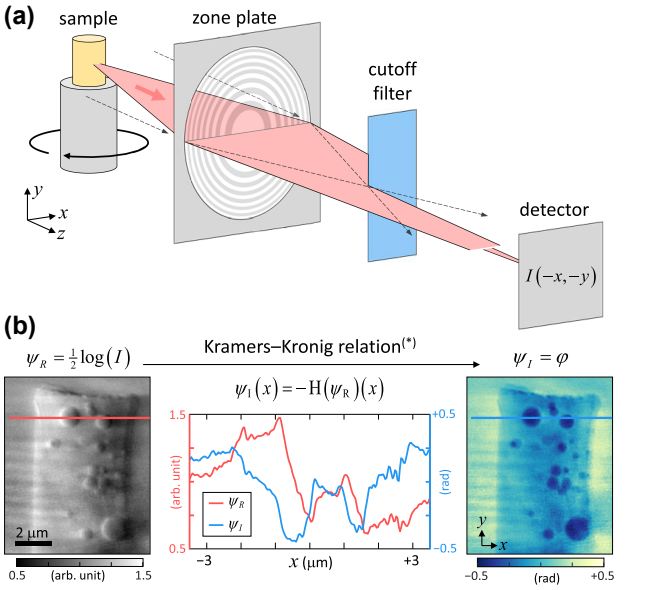

Fig. 1. Kramers–Kronig (KK) nanotomography. (a) Schematic setup of KK nanotomography. The incident field (dotted lines) and scattered field (red surfaces) are depicted. For improved visualization, only the X-rays on the horizontal plane ($y = 0$) are shown. (b) Phase retrieval via KK relations. From the acquired intensity image (I), the sample phase map (ϕ) is uniquely determined using the logarithm and Hilbert transform. (*)Note that the minus sign appears here in addition to Eq. (1) because the cutoff filter in (a) blocks the positive ($u > 0$) one-half of sample Fourier space, which is the opposite of the conventional definition of analytic signals.

of the sample field was presented. By cutting off one-half of the sample Fourier plane [$u > 0$ in Fig. 1(a)], we can confirm the analyticity of the transmitted sample field (U) and access the phase information using Eq. (1) [Fig. 1(b)]. Note that the analyticity of its logarithm $\psi = \log U$ can be derived from the analyticity of U based on the first-order Born approximation (see Supplement 1) [44,45]. Thus, enabling the space-domain KK relation [Eq. (1)] by introduction of the cutoff filter is the phase retrieval idea of this work. It should not be confused with Hilbert-transform-based filtering techniques of the filtered backprojection (FBP) method [46–48], which relates to the tomogram construction of scanned images rather than the phase retrieval of each scanned image.

Our cutoff method is more akin to the pupil modulation idea in electron microscopy [49] and optical microscopy [50] than interferometer-based [44,45], oblique-illumination-based [51,52], and diffraction-based [53] methods in optical microscopy. We dismissed the illumination-based schemes because they become ineffective for non-diffracting light such as X-rays [54]. It is also noteworthy that the introduction of a cutoff filter at the back-focal plane is similar to Foucault knife-edge scanning systems [55]. Despite the similarity of the optical setup, it needs to scan the cutoff filter laterally to calculate the phase gradient, whereas we do not have any mechanically moving parts except for sample rotation.

C. Intensity Modulation Ability of a Cutoff Filter

When we extract $\varphi(x)$ from $I(x)$ as described in Fig. 1, it means the cutoff filter somehow causes the sample phase to modulate the intensity. Then, what would be the conversion equation between the phase and intensity in the current system? This is an important

question for an intuitive understanding of the KK-relations-based phase reconstruction principle and estimation of the phase sensitivity of KK nanotomography.

To address the question, we analytically calculated the conversion equation under the weak absorption and phase shift condition similar to that of ZPC [24] (see Supplement 1),

$$I(x) \approx 1 + \log A(x) + \mathrm{H}(\Phi)(x), \tag{2}$$

where $A(x)$ and $\Phi(x)$ are the amplitude and phase shift images of a sample, respectively. Note that $\Phi(x)$ is the original sample phase before the cutoff filter and should not be confused with the phase of the transmitted sample field after the cutoff filter $\varphi(x)$. According to Eq. (2), we found the cutoff filter visualizes the Hilbert transform of $\Phi(x)$ and always produces intensity fluctuation comparable to the sample phase fluctuation according to the energy conservation property of Fourier transform [Eq. (S20)].

3. EXPERIMENTAL DETAILS

A. Setup

The experimental setup of the KK nanotomography is similar to that of existing TXM. Taking the advantage, the setup is prepared by simply replacing the phase plate of ZPC with a cutoff filter at the X-ray nanoimaging (7C XNI) beamline of the Pohang Light Source II (PLS-II) (Fig. 2) [22]. An off-axis zone plate imaging scheme was utilized to rule out the zeroth-order beam of the zone plate (Supplement 1, Fig. S1) [56].

An undulator source, optimized at 9.344 keV, was utilized. Horizontal and vertical adjustable slits were used to control the size of the source, which is closely related to the coherence length of the incident beam at the sample plane. We opened a $40\,(\mathrm{H}) \times 100\,(\mathrm{V})\ \mu\mathrm{m}^2$ aperture, which truncates only the horizontal size of the source as its original size is around $500\,(\mathrm{H}) \times 50\,(\mathrm{V})\ \mu\mathrm{m}^2$ according to [57]. A liquid-nitrogen-cooled silicon (111) double-crystal monochromator (DCM) (Vactron Co., Ltd., Republic of Korea) was utilized to obtain temporal coherence ($\Delta E/E \approx 10^{-4}$). A flat mirror was introduced to remove the harmonic frequencies.

A compound refractive lens (CRL) was used for focusing optics; it is composed of three beryllium lenses of 0.05 mm curvature radius (RXOPTICS GmbH, Germany). A 100 μm pinhole was placed in front of the sample to minimize unwanted diffraction noise. The sample was mounted on a precise rotation stage (RT150U; LAB Motion Systems). A zone plate of 300 μm with a 30 nm outermost zone width made of 700-nm-thick gold (Applied Nanotools Inc., Canada) was used. The zone plate was placed off-axis at 45 μm to evade the zeroth-order beam. The cutoff filter was a 1-mm-wide silicon (0.5-mm-thick) attached to an aluminum mount. Its flat surface was used as a cutoff boundary by aligning its width parallel to the beam direction. The calculated transmittance of the 1 mm silicon with respect to the X-ray energy (9.344 keV) was 0.011%.

A Tb:LSO scintillator ($Tb^{3+}:Lu_2SiO_5$, 17.0 μm thickness, $\lambda_{sc} = 542$ nm) on a YSO substrate (Yb_2SiO_5, 170 μm thickness) was used as an X-ray detector. An optical microscope equipped with a ×20 objective lens (NA = 0.4, LD Plan-Neofluar, ZEISS) was used to magnify the scintillator. An sCMOS camera (6.5 μm, 2048 × 2048, Zyla 4.2 PLUS, Oxford Instruments plc) was used as a detector. Because we used a 2 × 2 binned pixel, the effective pixel size of the camera was 13.0 μm. The magnification factor of the X-ray imaging system was calibrated by using a resolution target. The corresponding pixel size of the sample image was 36 nm. Because we did not alter the sampling rate during the tomogram reconstruction sequences, the voxel size of the tomograms was $36 \times 36 \times 36\ \mathrm{nm}^3$ throughout the course of the study.

B. 360° Angle Scan

Unlike in conventional tomography, a full 360° angle scan is required in KK nanotomography. This is because the θ and $\theta + 180°$ projections are no longer identical, instead, existing as complementary pairs acquiring the other half of the Fourier plane. Therefore, though we retrieve a filtered field image from a single acquisition, a complete field image can be acquired by merging the two field images into one piece (Supplement 1, Fig. S4). Compared with conventional phase nanotomography that typically require three acquisitions or more [30,58], the requirement of two acquisitions is a clear practical advantage of KK nanotomography. Moreover, because KK nanotomography does not require mechanical translations of samples as conventional phase nanotomography does, substantial practical advantages are expected, especially in setup stability and tomogram acquisition time.

The angle scanning step ($\delta\theta$) was determined based on $\delta\theta = 2\delta x/W$, where δx is the horizontal imaging resolution and W is the width of samples [54]. We obtained $\delta\theta = 2.2°$ for $W = 5$ μm and $\delta x = 100$ nm. The 360° angle scan was conducted with 1° angle steps. The number of projections was 361. We employed an alternative angle-scanning scheme; odd-numbered projections were acquired first, whereas even-numbered projections were acquired later. This scheme introduced a longer temporal gap between adjacent projection angles, helping correct the long-term drift in the following phase retrieval and image processing step. The acquisition time per projection was 2 s, resulting in a cumulative time of 12 min for tomogram acquisition and ~25 min overall (including sample rotation times between each acquisition). Following the angle scan and phase retrievals, we utilized the FBP method to build a sample tomogram. Detailed procedures can be found in Supplement 1.

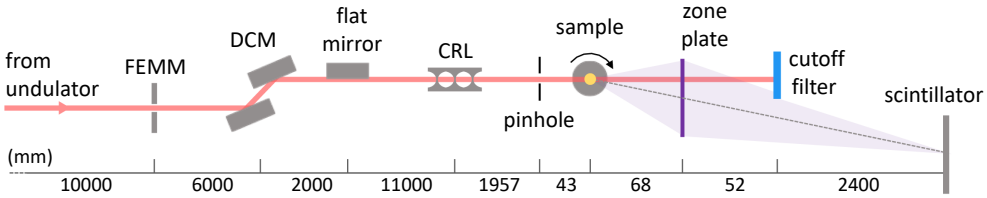

Fig. 2. Full configuration of used setup. The definitions of abbreviations are as follows: FEMM, front-end movable masks (horizontal and vertical adjustable slits); DCM, double-crystal monochromator; CRL, compound refractive lenses. The distances between the elements are denoted in millimeters.

4. RESULTS AND DISCUSSION

A. Tomogram Results

To validate the quantification performance of KK nanotomography, we first prepared a sample by mixing three different nanoparticles (silica, aluminum, and copper) with a commercial adhesive (see Supplement 1 for details on sample preparation).

The reconstructed tomogram of the sample is shown in Figs. 3(a)–3(d). The volumetric distributions of δ values are presented, where the X-ray refractive index is $n = 1 - \delta + i\beta$. The 3-D structure of the sample was visualized effectively, including the adhesive medium and embedded nanoparticles. To classify the nanoparticles, we compared the measured δ values with the known values of materials [Fig. 3(e), dotted lines] [5]. Using the density values provided by the manufacturer, we obtained the expected δ values of 5.75, 6.26, and 17.72 for silica, aluminum, and copper, respectively (in 10^{-6} units). As shown in Fig. 3(e), the measured values agree with the expected values. The mean (standard deviation) δ values of the aluminum and copper nanoparticles on the profile are 6.08 (0.44) and 17.39 (0.86) in 10^{-6} units. Some copper particles demonstrated smaller δ values (down to 15×10^{-6}), which could imply density variation in the nanoparticles.

Although copper is easily identified by its high δ values, distinguishing between silica and aluminum quantitatively is not straightforward because their expected δ difference (0.51×10^{-6}) is comparable to the standard deviation of background δvalues (0.38×10^{-6}). Silica and aluminum nanoparticles were instead distinguished based on their sizes, as shown in Fig. 3(a).

In our measurements, the background level is highly depending on the unwanted coherent diffractions (i.e., coherent noise) from dust on windows and a zone plate. Ideally, such coherent noise should be removed during the incident image division (or normalization) process (see Supplement 1), and the background level should only be determined on the shot and readout noises. However, the coherent noise is often time-varying due to the instability in practical imaging system and contributes to the background level. Note that this is a common issue in computed tomography and is a major cause of ring artifacts [59]. Fortunately, we found our KK-relations-based field reconstruction [Eq. (1)] is robust even in noisy situations due to the spectrum-conserving transfer function of Hilbert transform (see Supplement 1).

A commercially available tungsten tip (460-106, Ted Pella, Inc., United States) was used for the subsequent sample [Fig. 3(f)]. Because the sample was composed of a single material, we directly converted the measured δ values into local tungsten densities. The measured density was determined to be close to the single-crystalline density of tungsten (19.3 g cm^{-3}) at the apex and was gradually decreasing with a decrease in height. Uneven internal structures could also be observed, including long and narrow tunnels created along the direction of the height. It is noteworthy that the δ values are often directly converted to the electron density (ρ_e) using $\delta = r_e \lambda^2 \rho_e / (2\pi)$, where r_e is the classical electron radius and λ is the wavelength of the X-ray [12,32]. Such conversion is possible when the photon energy is sufficiently far from the absorption edges of the materials [4,9].

The spatial resolution of the current demonstrations is predominantly flux-limited. It depends on the diffraction power of a sample, the number of impinged photons, and the net photon detection ability of an X-ray imaging system. The achieved resolution can be deduced to be better than 100 nm based on the well-resolved minute crack on the tungsten tip [inset (iii) in Fig. 3(f), arrow]. In general, the theoretical resolution limits can be calculated from the imaging geometry and are expected to be asymmetric: 28 nm on the horizontal ($x - z$) plane and ~30 nm along the vertical (y) direction (see Supplement 1 for details). The enhancement of the horizontal resolution is expected owing to the off-axis geometry, which gathers higher-angle diffraction signals [22]. We expect that further optimization of coherent photon generation, diffraction, and detection will enable a closer approach to the theoretical resolution limits.

B. Comparison to ZPC Nanotomography

We also directly compared KK and ZPC nanotomography by observing identical samples using both methods. For the ZPC setup, we used the standard XNI configuration of the beamline [22]. The same X-ray energy (9.344 keV), focusing optics (CRL), and zone plate in the off-axis geometry were used. A phase plate was applied to the unmodulated term ($u = 0$) of the first-order diffraction. The phase plate is a 4-μm-diameter pinhole on a 960-nm-thick gold film. It induces $-\pi/2$ phase shift (at 9.344 keV) to the sample-modulated terms, which is identical to $+\pi/2$ relative phase shift on the unmodulated term. The 180° angle scan was conducted with 1° angle step. The number of projections was 301. The phase in ZPC is calculated by $\varphi(x) = (I(x) - 1)/2$ based on the derivation under the weak absorption and phase shift approximation [24]. Patterned silicon and an integrated circuit were prepared as samples (see Supplement 1).

The comparative results for the patterned silicon are shown in Figs. 4(a) and 4(b). Because the sample consisted of a pure silicon single crystal (100), it was expected to show a uniform δ value. In the KK tomogram, we can observe the homogenous structure of the sample as expected, although there is a certain level of fluctuation due to the unremoved ring artifacts [Fig. 4(a)]. Meanwhile, the ZPC tomogram does not reveal an accurate internal structure owing to halo and shade-off artifacts [Fig. 4(b)]. These artifacts originate in the physical size of the phase plate, which also modulates the low-frequency portion of scattered sample field [60]. These artifacts make the ZPC less sensitive to slowly varying structures, as shown in Fig. 4(b), which is critical for quantitative analysis. Even though the artifacts can be minimized by reducing the phase plate size [61], they remain an unresolved issue as it is practically difficult to fabricate and maintain such a high-aspect-ratio nanostructure.

The comparative results of the integrated circuit are shown in Figs. 4(c) and 4(d). In both the KK and ZPC results, the internal 3-D structure of the circuits was effectively visualized, despite the ZPC presenting consistently low δ values [Fig. 4(d)]. In the KK tomogram, it was possible to quantitatively differentiate between the various component materials [Fig. 4(c)]. In particular, high δ values provided useful insights to enable the exclusion of materials that cannot reach the δ value. For instance, the finest pin structures of the circuit exhibit a significantly larger δ than those of the other circuit structures [Fig. 4(e), red line]. Because the measured δ values are much larger than the expected δ of single-crystalline copper, we can deduce that the finest structures are composed of materials with larger atomic numbers [Fig. 4(e), arrows]. Based on previous studies of integrating circuits [33], we speculate that the structure is made of tungsten. However, in the ZPC tomogram result, the finest structures cannot be differentiated from the other circuit structures quantitatively [Fig. 4(e), arrows]. Such indistinguishability is a common fundamental vulnerability of ZPC.

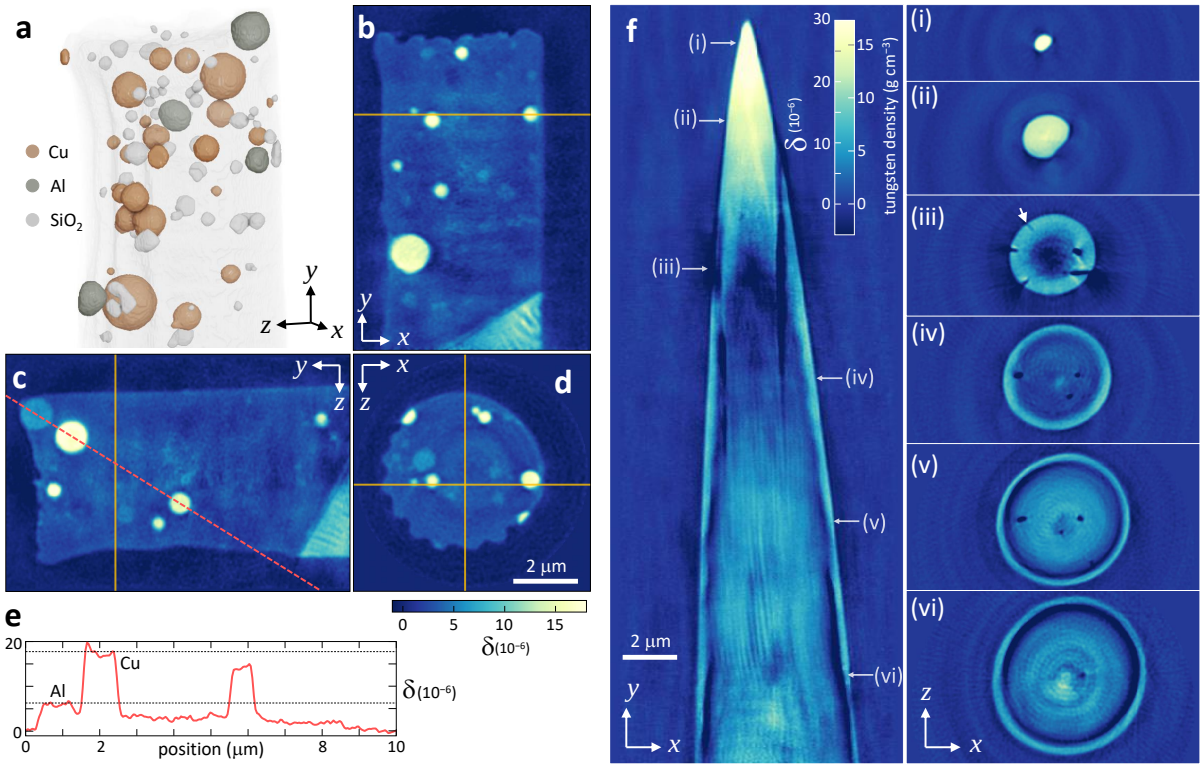

Fig. 3. Experimental sample tomogram results. (a) 3-D rendered image of the nanoparticle sample. The embedded nanoparticles are segmented based on measured δ values and sizes. (b)–(d) Representative orthogonal views of the tomogram. The orange lines indicate intersections between the cross sections. Unit vectors: $\hat{z}$, beam direction; $\hat{y}$, vertical (upward) direction; $\hat{x} = \hat{y} \times \hat{z}$, horizontal direction [as shown in Fig. 1(a)]. (e) Profile along the red dotted line in (c). The expected δ values of copper and aluminum are shown together. (f) The tomogram of a tungsten tip. The measured δ values can be directly interpreted as the local densities of tungsten. Axial cross sections are shown at various heights [(i)–(vi)] to better visualize the inhomogeneity of the sample. The arrow in (iii) indicates the resolved ~100 nm crack.

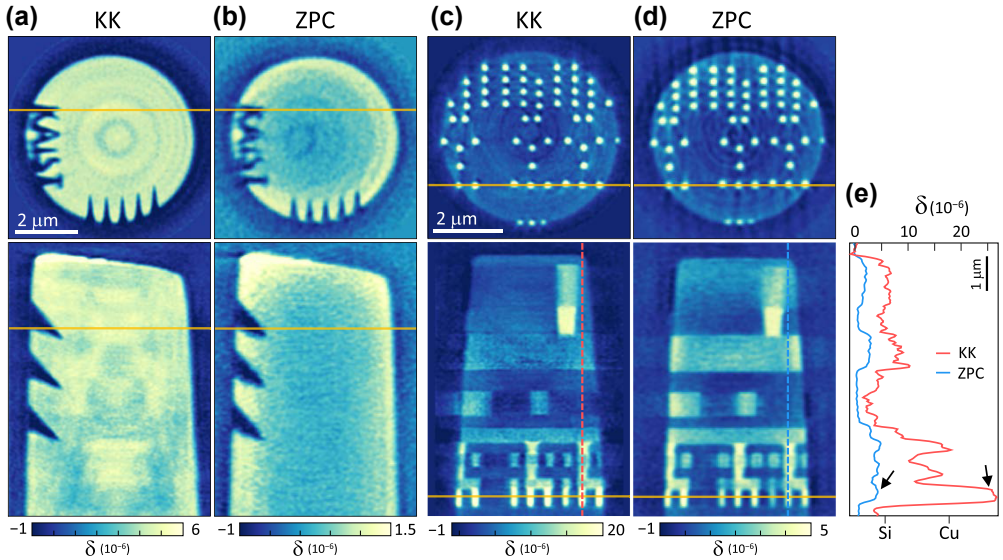

Fig. 4. Comparison with Zernike phase contrast (ZPC) nanotomography. (a)–(b) Tomograms of patterned silicon reconstructed by (a) KK and (b) ZPC schemes. (c)–(d) Tomograms of an integrated circuit reconstructed by (c) KK and (d) ZPC schemes. The orange lines indicate intersections between the cross sections. Note the inconsistency between the color scales of the KK and ZPC results owing to the systematically low δ values of ZPC. (e) Profiles along the dotted lines in (c) and (d). The expected δ values of copper and aluminum are marked below. Arrows emphasize the different sensitivities of the two methods with respect to δ variation.

Unfortunately, some ghost structures are shown around the sample [Fig. 4(c), arrow]. The ghost structures are originated from the phase reconstruction failure at a few projection angles that contain the circuit structures parallel to the beam direction (Supplement 1, Fig. S2). The large absorption and phase shift induced by the parallel structures could induce the local violation of the first-order

Born approximation, which is required to achieve the analyticity of $\log U$ (see Supplement 1).

C. Potential Issues

To facilitate the straightforward and rapid reproduction of KK nanotomography elsewhere, we clarify the potential issues that could fundamentally or practically impede the application.

First, we only retrieved the phase along the horizontal direction [the x direction in Fig. 1(a)]. Therefore, the phases between horizontal lines must be defined based on the known background area of the measured image. This may become an issue when the sample fully occupies the field of view. To achieve a two-dimensional (2-D) phase map directly, it is necessary to prepare a cutoff mask that satisfies 2-D analyticity [42,51]. However, we found that one-dimensional analyticity is sufficient in most situations because the background region is already required in the construction of the phase tomogram to determine the phases between the projection angles.

Second, sufficiently stable beam illumination is required during acquisition. In KK nanotomography, the position of the cutoff filter is crucial for accurate phase quantification. To achieve analyticity of the sample field U, the cutoff filter should block either $u > 0$ or $u < 0$ of the sample Fourier plane. However, to achieve the analyticity of $\log U$, the incident field (at $u = 0$) should not be blocked (see Supplement 1). Fortunately, positioning the filter at the right position is not difficult because the alignment process is almost identical to the Foucault knife-edge test [62]. However, such strict requirements on the filter position can be problematic when the beam illumination angle fluctuates during the angle-scanning sequence.

Third, the proposed method requires the full spatial coherence of the sample. Although the coherence can always be achieved by sufficient spatial filtering or beam broadening, it often significantly reduces the beam flux. Because the beam flux is directly related to the resolution and quality of the tomogram results, the determination of an adequate coherence length represents an important practical issue. In this study, we prepared a sample width of $\sim$5 μm, which is sufficiently smaller than the calculated horizontal coherence length ($\sim$10 μm) of the given configuration. Thus, we expect KK nanotomography to become much more powerful with upcoming diffraction-limited storage rings [63].

5. CONCLUSION

We have proposed and demonstrated a novel quantitative X-ray phase nanotomography technique that exploits the space-domain KK relation. By introducing a cutoff filter to the conventional TXM setup, we showed that the transmitted phase map can directly be calculated from a single intensity image. Because KK nanotomography requires only two acquisitions (θ and $\theta + 180°$ projections) for phase retrieval without mechanical translation of samples, we expect it is practically advantageous over existing phase nanotomography in terms of setup stability and tomogram acquisition time.

The phase quantification capability was demonstrated in various samples. The local material composition or local density were identified by the measured δ. We expect the δ quantitation capability would be advantageous for composite material studies such as lithium-ion battery materials [2,34,64].

To enable further development, X-ray energy scanning can also be introduced to the KK nanotomography. Taking advantage of the achromatic feature of a cutoff filter, quantitative phase tomograms can be acquired at various X-ray energies without a major change in the setup. Such spectral analyses of the 3-D distribution of δ values would provide useful information on the compositions and states of the samples [65].

Funding. Institute for Information and Communications Technology Promotion (2021-0-00745); Ministry of Science and ICT, South Korea (N11210014, N11220131); National Research Foundation of Korea (2015R1A3A2066550, 2018R1A6B4023605, 2021R1C1C2009220); Tomocube Inc.; Ministry of Trade, Industry and Energy (20011661); Pohang University of Science and Technology (POSTECH).

Acknowledgment. Experiments using PLS-II were supported in part by MSIT and POSTECH. The samples were prepared at KAIST Analysis Center for Research Advancement (KARA).

Disclosures. The authors declare no conflicts of interest.

Data availability. Data underlying the results presented in this paper are not publicly available at this time but may be obtained from the authors upon reasonable request.

Supplemental document. See Supplement 1 for supporting content.

REFERENCES

1. P. J. Withers, "X-ray nanotomography," Mater. Today **10**(12), 26–34 (2007).
2. P. Pietsch and V. Wood, "X-ray tomography for lithium ion battery research: a practical guide," Annu. Rev. Mater. Res. **47**, 451–479 (2017).
3. M. Ge, D. S. Coburn, E. Nazaretski, W. Xu, K. Gofron, H. Xu, Z. Yin, and W.-K. Lee, "One-minute nano-tomography using hard x-ray full-field transmission microscope," Appl. Phys. Lett. **113**, 083109 (2018).
4. D. Attwood and A. Sakdinawat, *X-Rays and Extreme Ultraviolet Radiation: Principles and Applications* (Cambridge University, 2017).
5. B. L. Henke, E. M. Gullikson, and J. C. Davis, "X-ray interactions: photoabsorption, scattering, transmission, and reflection at E = 50-30,000 eV, Z = 1-92," At. Data Nucl. Data Tables **54**, 181–342 (1993).
6. P. Cloetens, R. Barrett, J. Baruchel, J.-P. Guigay, and M. Schlenker, "Phase objects in synchrotron radiation hard x-ray imaging," J. Phys. D **29**, 133–146 (1996).
7. S. W. Wilkins, T. E. Gureyev, D. Gao, A. Pogany, and A. W. Stevenson, "Phase-contrast imaging using polychromatic hard x-rays," Nature **384**, 335–338 (1996).
8. K. A. Nugent, "Coherent methods in the x-ray sciences," Adv. Phys. **59**, 1–99 (2010).
9. A. Diaz, P. Trtik, M. Guizar-Sicairos, A. Menzel, P. Thibault, and O. Bunk, "Quantitative x-ray phase nanotomography," Phys. Rev. B **85**, 020104 (2012).
10. A. Momose, T. Takeda, and Y. Itai, "Phase-contrast x-ray computed tomography for observing biological specimens and organic materials," Rev. Sci. Instrum. **66**, 1434–1436 (1995).
11. F. Pfeiffer, C. Kottler, O. Bunk, and C. David, "Hard X-ray phase tomography with low-brilliance sources," Phys. Rev. Lett. **98**, 108105 (2007).
12. P. Cloetens, W. Ludwig, J. Baruchel, D. V. Dyck, J. V. Landuyt, J. P. Guigay, and M. Schlenker, "Holotomography: quantitative phase tomography with micrometer resolution using hard synchrotron radiation X-rays," Appl. Phys. Lett. **75**, 2912–2914 (1999).
13. P. J. McMahon, A. G. Peele, D. Paterson, J. J. A. Lin, T. H. K. Irving, I. McNulty, and K. A. Nugent, "Quantitative x-ray phase tomography with sub-micron resolution," Opt. Commun. **217**, 53–58 (2003).
14. P. J. McMahon, A. G. Peele, D. Paterson, K. A. Nugent, A. Snigirev, T. Weitkamp, and C. Rau, "X-ray tomographic imaging of the complex refractive index," Appl. Phys. Lett. **83**, 1480–1482 (2003).
15. A. Khimchenko, C. Bikis, A. Pacureanu, S. E. Hieber, P. Thalmann, H. Deyhle, G. Schweighauser, J. Hench, S. Frank, M. Müller-Gerbl, G. Schulz, P. Cloetens, and B. Müller, "Hard x-ray nanoholotomography: large-scale, label-free, 3D neuroimaging beyond optical limit," Adv. Sci. **5**, 1700694 (2018).

16. I. Zanette, T. Zhou, A. Burvall, U. Lundström, D. H. Larsson, M. Zdora, P. Thibault, F. Pfeiffer, and H. M. Hertz, "Speckle-based x-ray phase-contrast and dark-field imaging with a laboratory source," Phys. Rev. Lett. **112**, 253903 (2014).
17. M.-C. Zdora, P. Thibault, W. Kuo, V. Fernandez, H. Deyhle, J. Vila-Comamala, M. P. Olbinado, A. Rack, P. M. Lackie, O. L. Katsamenis, M. J. Lawson, V. Kurtcuoglu, C. Rau, F. Pfeiffer, and I. Zanette, "X-ray phase tomography with near-field speckles for three-dimensional virtual histology," Optica **7**, 1221–1227 (2020).
18. M. Stampanoni, R. Mokso, F. Marone, J. Vila-Comamala, S. Gorelick, P. Trtik, K. Jefimovs, and C. David, "Phase-contrast tomography at the nanoscale using hard X-rays," Phys. Rev. B **81**, 140105 (2010).
19. G. Schmahl, D. Rudolph, G. Schneider, P. Guttmann, and B. Niemann, "Phase contrast x-ray microscopy studies," Optik **97**, 181–182 (1994).
20. J. C. Andrews, S. Brennan, C. Patty, K. Luening, P. Pianetta, E. Almeida, M. C. H. van der Meulen, M. Feser, J. Gelb, J. Rudati, A. Tkachuk, and W. B. Yun, "A high resolution, hard x-ray bio-imaging facility at SSRL," Synchrotron Radiat. News **21**, 17–26 (2008).
21. M. Ogurreck, F. Wilde, J. Herzen, F. Beckmann, V. Nazmov, J. Mohr, A. Haibel, M. Müller, and A. Schreyer, "The nanotomography endstation at the PETRA III imaging beamline," J. Phys. Conf. Ser. **425**, 182002 (2013).
22. J. Lim, H. Kim, and S. Y. Park, "Hard x-ray nanotomography beamline 7C XNI at PLS-II," J. Synchrotron Radiat. **21**, 827–831 (2014).
23. D. S. Coburn, E. Nazaretski, W. Xu, M. Ge, C. Longo, H. Xu, K. Gofron, Z. Yin, H. H. Chen, Y. Hwu, and W.-K. Lee, "Design, characterization, and performance of a hard x-ray transmission microscope at the National Synchrotron Light Source II 18-ID beamline," Rev. Sci. Instrum. **90**, 053701 (2019).
24. Y. Yang, R. Heine, Y. Cheng, C.-C. Wang, Y.-F. Song, and T. Baumbach, "Approaching quantitative Zernike phase contrast in full-field transmission hard x-ray microscopy: origin and reduction of artifacts," Appl. Phys. Lett. **105**, 094101 (2014).
25. H. Chen, Z. Wang, K. Gao, Q. Hou, D. Wang, and Z. Wu, "Quantitative phase retrieval in x-ray Zernike phase contrast microscopy," J. Synchrotron Radiat. **22**, 1056–1061 (2015).
26. S. Y. Park, C. K. Hong, and J. Lim, "A method of hard x-ray phase-shifting digital holography," J. Synchrotron Radiat. **23**, 1024–1029 (2016).
27. G. Schmahl and D. Rudolph, "Proposal for a phase contrast x-ray microscope," in *X-Ray Microscopy: Instrumentation and Biological Applications*, P.-C. Cheng and G.-J. Jan, eds. (Springer, 1987), pp. 231–238.
28. R. Mokso, P. Cloetens, E. Maire, W. Ludwig, and J.-Y. Buffière, "Nanoscale zoom tomography with hard X-rays using Kirkpatrick-Baez optics," Appl. Phys. Lett. **90**, 144104 (2007).
29. S. Flenner, A. Kubec, C. David, M. Storm, C. F. Schaber, F. Vollrath, M. Müller, I. Greving, and J. Hagemann, "Hard x-ray nano-holotomography with a Fresnel zone plate," Opt. Express **28**, 37514–37525 (2020).
30. M. Langer, P. Cloetens, J.-P. Guigay, and F. Peyrin, "Quantitative comparison of direct phase retrieval algorithms in in-line phase tomography," Med. Phys. **35**, 4556–4566 (2008).
31. S. Zabler, P. Cloetens, J.-P. Guigay, J. Baruchel, and M. Schlenker, "Optimization of phase contrast imaging using hard X-rays," Rev. Sci. Instrum. **76**, 073705 (2005).
32. M. Dierolf, A. Menzel, P. Thibault, P. Schneider, C. M. Kewish, R. Wepf, O. Bunk, and F. Pfeiffer, "Ptychographic x-ray computed tomography at the nanoscale," Nature **467**, 436–439 (2010).
33. M. Holler, M. Guizar-Sicairos, E. H. R. Tsai, R. Dinapoli, E. Müller, O. Bunk, J. Raabe, and G. Aeppli, "High-resolution non-destructive three-dimensional imaging of integrated circuits," Nature **543**, 402–406 (2017).
34. E. H. R. Tsai, J. Billaud, D. F. Sanchez, J. Ihli, M. Odstrčil, M. Holler, D. Grolimund, C. Villevieille, and M. Guizar-Sicairos, "Correlated x-ray 3D ptychography and diffraction microscopy visualize links between morphology and crystal structure of lithium-rich cathode materials," iScience **11**, 356–365 (2019).
35. M. Holler and J. Raabe, "Error motion compensating tracking interferometer for the position measurement of objects with rotational degree of freedom," Opt. Eng. **54**, 054101 (2015).
36. M. Hirose, K. Shimomura, N. Burdet, and Y. Takahashi, "Use of Kramers–Kronig relation in phase retrieval calculation in x-ray spectro-ptychography," Opt. Express **25**, 8593–8603 (2017).
37. D. B. Tanner, "Use of x-ray scattering functions in Kramers-Kronig analysis of reflectance," Phys. Rev. B **91**, 035123 (2015).
38. J. R. Fienup, "Phase retrieval algorithms: a comparison," Appl. Opt. **21**, 2758–2769 (1982).
39. T. E. Gureyev, A. Roberts, and K. A. Nugent, "Partially coherent fields, the transport-of-intensity equation, and phase uniqueness," J. Opt. Soc. Am. A **12**, 1942–1946 (1995).
40. E. J. Candès, X. Li, and M. Soltanolkotabi, "Phase retrieval via Wirtinger flow: theory and algorithms," IEEE Trans. Inf. Theory **61**, 1985–2007 (2015).
41. K. Lee and Y. Park, "Exploiting the speckle-correlation scattering matrix for a compact reference-free holographic image sensor," Nat. Commun. **7**, 13359 (2016).
42. J. P. Havlicek, J. W. Havlicek, and A. C. Bovik, "The analytic image," in *International Conference on Image Processing* (1997), Vol. **442**, pp. 446–449.
43. J. S. Toll, "Causality and the dispersion relation: logical foundations," Phys. Rev. **104**, 1760–1770 (1956).
44. C. S. Seelamantula, N. Pavillon, C. Depeursinge, and M. Unser, "Exact complex-wave reconstruction in digital holography," J. Opt. Soc. Am. A **28**, 983–992 (2011).
45. Y. Baek, K. Lee, S. Shin, and Y. Park, "Kramers–Kronig holographic imaging for high-space-bandwidth product," Optica **6**, 45–51 (2019).
46. Z.-F. Huang, K.-J. Kang, Z. Li, P.-P. Zhu, Q.-X. Yuan, W.-X. Huang, J.-Y. Wang, D. Zhang, and A.-M. Yu, "Direct computed tomographic reconstruction for directional-derivative projections of computed tomography of diffraction enhanced imaging," Appl. Phys. Lett. **89**, 041124 (2006).
47. J. You and G. L. Zeng, "Hilbert transform based FBP algorithm for fan-beam CT full and partial scans," IEEE Trans. Med. Imaging **26**, 190–199 (2007).
48. L. Li, K. Kang, Z. Chen, L. Zhang, and Y. Xing, "A general region-of-interest image reconstruction approach with truncated Hilbert transform," J. X-Ray Sci. Technol. **17**, 135–152 (2009).
49. D. L. Misell, R. E. Burge, and A. H. Greenaway, "Alternative to holography for determining phase from image intensity measurements in optics," Nature **247**, 401–402 (1974).
50. C. Shen, M. Liang, A. Pan, and C. Yang, "Non-iterative complex wavefield reconstruction based on Kramers–Kronig relations," Photon. Res. **9**, 1003–1012 (2021).
51. Y. Baek and Y. Park, "Intensity-based holographic imaging via space-domain Kramers–Kronig relations," Nat. Photonics **15**, 354–360 (2021).
52. C. Lee, Y. Baek, H. Hugonnet, and Y. Park, "Single-shot wide-field topography measurement using spectrally multiplexed reflection intensity holography via space-domain Kramers–Kronig relations," Opt. Lett. **47**, 1025–1028 (2022).
53. J. Li, N. Zhou, J. Sun, S. Zhou, Z. Bai, L. Lu, Q. Chen, and C. Zuo, "Transport of intensity diffraction tomography with non-interferometric synthetic aperture for three-dimensional label-free microscopy," Light Sci. Appl. **11**, 154 (2022).
54. A. C. Kak and M. Slaney, *Principles of Computerized Tomographic Imaging* (Society for Industrial and Applied Mathematics, 2001).
55. N. Watanabe, Y. Tsuburaya, A. Shimada, and S. Aoki, "Quantitative phase tomography by using x-ray microscope with Foucault knife-edge scanning filter," AIP Conf. Proc. **1696**, 020044 (2016).
56. J. Lim, S. Y. Park, J. Y. Huang, S. M. Han, and H.-T. Kim, "Large-field high-contrast hard x-ray Zernike phase-contrast nano-imaging beamline at Pohang Light Source," Rev. Sci. Instrum. **84**, 013707 (2013).
57. S. Y. Park, C. K. Hong, and J. Lim, "Measurement of coherence length and incoherent source size of hard x-ray undulator beamline at Pohang Light Source-II," Rev. Sci. Instrum. **85**, 045116 (2014).
58. O. Bunk, M. Dierolf, S. Kynde, I. Johnson, O. Marti, and F. Pfeiffer, "Influence of the overlap parameter on the convergence of the ptychographical iterative engine," Ultramicroscopy **108**, 481–487 (2008).
59. B. Münch, P. Trtik, F. Marone, and M. Stampanoni, "Stripe and ring artifact removal with combined wavelet and Fourier filtering," Opt. Express **17**, 8567–8591 (2009).
60. C. Edwards, B. Bhaduri, T. Nguyen, B. G. Griffin, H. Pham, T. Kim, G. Popescu, and L. L. Goddard, "Effects of spatial coherence in diffraction phase microscopy," Opt. Express **22**, 5133–5146 (2014).
61. I. Vartiainen, R. Mokso, M. Stampanoni, and C. David, "Halo suppression in full-field x-ray Zernike phase contrast microscopy," Opt. Lett. **39**, 1601–1604 (2014).

62. E. P. Goodwin and J. C. Wyant, *Field Guide to Interferometric Optical Testing* (SPIE, 2006).
63. M. Eriksson, J. F. van der Veen, and C. Quitmann, "Diffraction-limited storage rings—a window to the science of tomorrow," J. Synchrotron Radiat. **21**, 837–842 (2014).
64. Z. Jiang, J. Li, Y. Yang, L. Mu, C. Wei, X. Yu, P. Pianetta, K. Zhao, P. Cloetens, F. Lin, and Y. Liu, "Machine-learning-revealed statistics of the particle-carbon/binder detachment in lithium-ion battery cathodes," Nat. Commun. **11**, 2310 (2020).
65. J. Zhang, Q. Wang, S. Li, Z. Jiang, S. Tan, X. Wang, K. Zhang, Q. Yuan, S.-J. Lee, C. J. Titus, K. D. Irwin, D. Nordlund, J.-S. Lee, P. Pianetta, X. Yu, X. Xiao, X.-Q. Yang, E. Hu, and Y. Liu, "Depth-dependent valence stratification driven by oxygen redox in lithium-rich layered oxide," Nat. Commun. **11**, 6342 (2020).

143.248.11.147 {ts '2023-04-07 03:06:19'}